Journal of The Electrochemical Society, 2020 **167** 144502

Hydrophobic, Carbon Free Gas Diffusion Electrode for Alkaline Applications

Artur Bekisch,[1,2] Karl Skadell,[1] David Poppitz,[3] Matthias Schulz,[1] Roland Weidl,[1] and Michael Stelter[1,2,z]

[1]*Fraunhofer Institute for Ceramic Technologies and Systems IKTS, 07629 Hermsdorf, Germany*
[2]*Center for Energy and Environmental Chemistry Jena, Friedrich-Schiller-University Jena, 07743 Jena, Germany*
[3]*Institute of Chemical Technology, University Leipzig, 04103 Leipzig, Germany*

In this work we present a carbon free gas diffusion electrode (GDE) design. It is a first step towards improvement of technologies like alkaline fuel cells, some alkaline electrolyzes and metal-air-batteries by circumventing carbon degradation. A nickel-mesh was made hydrophobic and subsequently electrochemically coated with MnO_x as electrocatalyst. By this, a carbon free GDE was prepared. The contact angle, specific surface area (BET), pore size distribution, crystal phase (XRD) and electrochemical properties were determined. The deposition scan rate (r_{scan}) during dynamic MnO_x deposition altered the macro surface structure, pore size distribution and deposited mass. High catalyst masses with high specific surface area were achieved by lower r_{scan}, but hydrophobicity was decreased. Impedance spectroscopy showed that higher MnO_x mass will increase the ohmic resistance, because of the low conductivity of oxides, such as MnO_x. The diffusion of dissolved oxygen is the major contributor to the total resistance. However, the polarization resistance was reduced by increased specific surface area of MnO_x. It was concluded that the ORR and OER are limited by diffusion in this design but nevertheless showed reasonable activity for ± 10 mA cm^{-2} corresponding to $\sim 8\ \Omega\ cm^{-2}$ while references exhibited $\sim 3.5\ \Omega\ cm^{-2}$.

[DOI: 10.1149/1945-7111/abbdd4]

Manuscript submitted January 28, 2020; revised manuscript received September 21, 2020. Published October 27, 2020.

Supplementary material for this article is available online

The application of gas diffusion electrodes (GDE) are of huge importance in many technologies like alkaline fuel cells,[1] some alkaline electrolyzes[2] and metal-air-batteries.[3] Novel components are investigated to reach higher cost-efficiency, environmental friendliness and higher energy density.[4–6] Catalysts for the oxygen reduction reaction (ORR) and oxygen evolution reaction (OER) play a key role in those technologies. Various perovskites, spinel or metal-free catalysts are used to overcome the dependency of precious metals like platinum or palladium.[7,8] Manganese oxide (MnO_x) is an attractive and widely used material in the field of electrochemistry. This is because of its low toxicity, high abundance, low material-cost and various crystal phases.[8] It was investigated intensively in different applications like supercapacitor, various catalysts combinations and cathode material for batteries.[8–12] MnO_x provides a rich stoichiometric and crystalline diversity. Additionally, some of them like MnO_2, Mn_2O_3 and Mn_3O_4 have shown a reasonable activity in ORR and OER.[13,14] Nickel is known as a catalyst for hydrogen evolution reactions (HER) and OER and achieves relatively low overpotentials.[15–17] The combination of both materials are beneficial for an electrochemical system which depends on a high ORR and OER activity.

The ORR follows two possible reaction pathways. The four-electron and two-electron pathway. However, the first one is more preferable due to hydrogen peroxide formation generated at the two-electron pathway. The latter one leads to corrosive effects and low energy efficiency.[18] This effects are severe on carbonaceous materials because carbon corrosion was found to lead to unstable behavior during OER.[5,10–12,19] For the OER pathway there are five possible reaction pathways in alkaline solution which were summarized by *Schmidt*'*s* group.[13] The mentioned decomposition of carbon occurs due to charging and discharging processes in an electrochemical system like metal air batteries. Therefore, performance, efficiency and durability of carbonaceous GDE decrease over time.[20,21] A state of the art GDE consist of porous carbon which is mixed with platin particles and PTFE. Carbon provides the electrical conductivity to the platin catalyst and PTFE creates a hydrophilic—hydrophobic pore system for gas and liquid electrolyte.

A straightforward approach to solve this carbon degradation is the application of electrodeposited catalyst on conductive metal meshes or foams. Thus, it is possible to improve the durability and performance of GDE by this binder- and carbon-free configuration.[22] There are several possibilities to adjust the electrodeposition to achieve the preferred coating for the specific application.

For example, *Tsai*'*s* group[11] prepared a MnO_2/Ni—foam as asymmetric supercapacitor by evaluating the potentiostatic, the potentiodynamic and the combination of both deposition modes. Satisfying results with increased porous surface area were achieved by the combination of both modes. Chou et al.[10] described the combination of potentiostatic and cyclic voltammetric technique to achieve a nanostructured γ-MnO_2 films on nickel sheets. They used it in electrochemical supercapacitor and primary alkaline Zn/MnO_2 batteries and reached a high specific capacitance of 240 F g^{-1} and a discharge current density of 500 mA g^{-1}. *Xu*'*s* group[23] synthesized MnO_2 nanospheres on nickel foam via hydrothermal method. The manufactured Ni/MnO_2 electrode was filled with a mixture of CNTs and PTFE and additionally a PTFE membrane was provided as a gas diffusion layer on one side of the electrode. This GDE was tested at a Zinc-air battery and exhibited a peak power density of 95.7 mW cm^{-2} and unchanged discharge stability. The group of *Ng*[22] deposited electrochemically MnO_x on stainless steel mesh. This coated mesh was electrochemically characterized with a rotating disc electrode (RDE) and showed high activities for ORR and OER and displays for 100 cycles high stability. Additionally, it showed its potential for fuel cells and metal-air batteries as carbon free GDE.

In this work, a bifunctional carbon free GDE for OER and ORR in alkaline media was established. This hybrid of nickel mesh and electrochemically deposited high surface area manganese oxide as an electrocatalyst was investigated.

This carbon free GDE configuration was inspired by *Ng*'*s* group[22] to electrochemically coat a nickel-mesh with a catalyst and by *Tsai*'*s* group[11] to vary the electrochemical deposition scan rate. This combination has been expanded by the introduction of a hydrophobic treatment to provide a novel carbon free GDE

[z]E-mail: michael.stelter@ikts.fraunhofer.de

configuration. The hydrophobic, carbon free GDE was investigated towards the influence of hydrophobic treatment and deposition scan rate (r_{scan}) of MnO_x. By combining of etching, heat treatment and the use of a fatty acid a hydrophobic nickel-mesh was achieved. Hereinafter, the mesh was coated with a bifunctional catalyst. This electrodeposition of MnO_x is the last step to establish a high surface GDE. The prepared carbon free GDEs were characterized regarding contact angle, specific surface area (nitrogen sorption (BET)), crystal reflexes (XRD), pore distribution, impedance spectroscopy and galvanostatic measurements. The electrochemical measurements were carried out with a symmetric cell setup being comprised of air/GDE/electrolyte/GDE/air. This setup was chosen to utilize an application-closer environment in comparison to RDE (ring disk electrode) measurement since they lack of a three phase boundary.

Experimental

Material.—Nickel-mesh (0.1 mm wire diameter; 0.15 mm mesh size; 36 mm^2 open sieve surface) was purchased from *Willy Kaldenbach KG*, Germany. Potassium hydroxide was purchased from *Merck KGaA*, Germany. Hydrochloric acid was purchased from *VWR International*, LLC, USA. Manganese (II) acetate tetra hydrate, sodium sulfate and stearic acid were purchased from *Carl Roth GmbH + Co. KG*, Germany. Commercial GDE (product name: MOC) was purchased from *Gaskatel Gesellschaft für Gassysteme durch Katalyse und Elektrochemie mbH*, Germany. All reagents were of analytical grade and used as received without further purification.

Hydrophobic treatment.—The hydrophobic treatment was established on basis of *Jie's*[24] and *Liu's*[25] work. Nickel-mesh samples (24 mm diameter) were cleaned ultrasonically in acetone for 30 min and dried in air. Cleaned samples were etched ultrasonically in 2 M HCl for 50 min, washed in deionized water and ethanol and then dried again. Furthermore, the nickel samples were heat treated in air at 350 °C for 20 min. Finally, the mesh surface is immersed for ten seconds in an ethanol solution of 10% stearic acid at room temperature and dried.

Electrodeposition protocol.—MnO_x was electrochemically deposited onto a hydrophobic nickel-mesh. The composition of the aqueous deposition electrolyte consisted of 0.1 M manganese (II) acetate tetra hydrate and 0.1 M sodium sulfate. The deposition was conducted in a beaker at a temperature of 30 °C. According to *Pourbaix*'[26] diagram of manganese the electrochemical settings were adjusted to obtain MnO_x with the oxidation number between 3 and 4. The working electrode was a nickel-mesh, a platinum electrode was used as counter electrode and a saturated calomel electrode (SCE) was used as reference electrode. The electrodeposition consists of two steps. Firstly, the potentiostatic deposition at 0.6 V for 15 min, and hereinafter, potentiodynamic deposition between 0.3 V and 0.6 V at a certain scan rate (r_{scan}) (12.5 mV s^{-1}, 25 mV s^{-1}, 37.5 mV s^{-1} and 50 mV s^{-1}) for 500 cycles was carried out. The meshes were coated at different r_{scan} to investigate its influence further. Finally, the electrode was dried in a drying oven at 120 °C. All samples and their characteristics are listed in Table I.

Surface characterization.—Field emission scanning electron microscopy (FESEM) ULTRA PLUS with a 2.0 kV beam current from *Carl Zeiss Microscopy GmbH* was used to investigate the morphology of the electrodes. An extra high tension (EHT) of 2.0 kV beam, 4.5 mm gun-to-sample distance and Signal A = InLens was used for 100 nm range and 10.0 kV beam, 8.2 mm gun-to-sample distance and Signal A = InLens was used for 100 μm range.

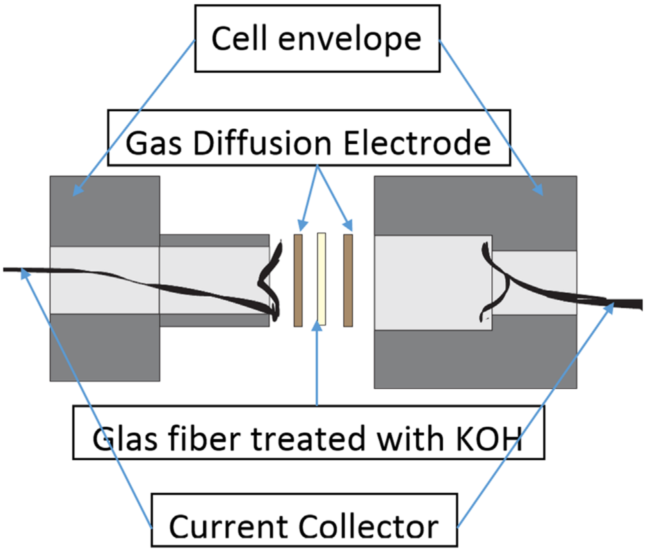

Figure 1. Schematic depiction of the symmetric cell assembly in a sectional top view.

Energy dispersive spectroscopy (EDS) from *EDAX Bussiness Unit AMETEK GmbH* was used to determine the elemental composition. Therefore, the used energy was 10 kV, the spot size was approx. 1–2 μm, the count time was 50 s and the detection limit was 0.3 wt.-%.

X-ray diffraction (XRD) analysis was carried out with a D8 Advance Bruker and a Cu-kα radiation from *Bruker Corporation*. MnO_x was electrochemically deposited on a nickel sheet at r_{scan} of 12.5 mV s^{-1} and afterwards scrapped off the nickel surface. This MnO_x was measured from 5° to 90° 2Θ with a velocity of 0.01° per 57.6 s.

Transmission electron microscopy (TEM) was carried out with a Jeol JEM2100Plus at a high tension of 200 kV. The MnO_x sample was made in the same way like at the XRD analysis. This sample was mortared in ethanol for two minutes. After 10 min of segregation a droplet was placed on a carbon TEM grid.

Lattice constants (respectively interplanar distance d) were calculated out of measured XRD pattern reflexes (2 Θ) by the Bragg's law (1).

$$n\lambda = 2d\,\sin(\Theta) \qquad [1]$$

n is a positive integer and λ is the wavelength of the incident wave (Cu_k$_\alpha$ radiation).

Contact angle measurements with the Contact Angle System OCAH200 from *DataPhysics Instrument GmbH* were used to analyze the hydrophobicity of samples. Droplets of 5 μl deionized water were put on the sample surface and after 3 to 5 s the Contact Angle System OCAH200 camera toke a digital photo. This

Table I. Sample overview.

Sample Name	Ni	Scr1	Scr2	Scr3	Scr4	GDE_{ref}	MnO_x
Hydrophobization	yes	yes	yes	yes	yes	n.d.[a)]	n.d.[a)]
MnO_x Deposition	n.d.[a)]	yes	yes	yes	yes	n.d.[a)]	yes
r_{scan}/mV s^{-1}	/	12.5	25	37.5	50	/	50

a) n.d.: not done.

procedure was carried out at three different locations of the same sample. The computer program of Contact Angle Systems OCAH200 (SCA20 Version 2) analyzed the formed contact angle of the droplet. All measured samples are shown in Table I. Sample Ni is a hydrophobic uncoated nickel mesh and sample MnO_x is a coated nickel sheet, which was not made hydrophobic.

The specific surface area was determined by nitrogen sorption method or *Brunauer-Emmet-Teller* (BET) measurement, respectively, with the ASAP2020 from *Micromeritics GmbH*. The adsorption of nitrogen was started by the steady increase of nitrogen-pressure and desorption was initiated by the steady decrease of nitrogen-pressure. The quantity of adsorbed and desorbed nitrogen was measured. The *Brunauer-Emmet-Teller* model was used to determine the specific surface area out of the measured adsorption and desorption data. The pore size distribution was analyzed with the micropore analysis method (MP-Method).

Electrochemical characterization.—A potentiostat SP-240 from *Bio-Logic Science Instruments* and a symmetric cell (self-designed) assembly was used to characterize the electrode. The electrochemical behavior was investigated using impedance spectroscopy and galvanostatic cycling. The symmetric cell assembly consisted of two identical electrodes separated by a glass fiber fleece soaked in 0.1 M KOH (Fig. 1). Nickel-mesh was used as current collectors, which were on both opposite sides of the openings. The screwing of the two symmetric cell parts pressed the two electrode samples and the soaked glass fiber fleece in the middle together. This ensured the ionic contact due to the electrolyte (KOH) which is inside of the glass fiber fleece. Thus, the pressure of the screwing guaranteed the wetting of the samples. The symmetric cell was in a horizontal position during all measurements to ensure that both sides are equally wetted. On both opposite sides in the screwed condition of the symmetric cell are openings that served as access to airside. The impedance spectroscopy was measured at a frequency range from 1 MHz to 5 mHz at OCV (open circuit voltage). Galvanostatic cycling was carried out applying 10 mA cm^{-2}, for a minimum of four cycles with each cycle lasting at least 5 min. The electrochemical available specific surface area and specific capacitance was measured with cyclic voltammetry (CV) at a potential-window of 0.32 V and 0.42 V. The samples were cycled at different scan rates (5, 10, 15, 20, 30 and 40 mA s^{-1}). The fitted slope results of the CV measurements were calculated with the constant capacitance[10] of 20 μF cm^{-2} to calculate the surface area. The electrolyte was 0.1 M KOH (12.7 pH), which results in a standard electrode potential of 0.37 V vs Hg/HgO 1 M NaOH. For this CV a half-cell assembly from *Gaskatel Gesellschaft für Gassysteme durch Katalyse und Elektrochemie mbH* was used (Fig. A6 is available online at stacks.iop.org/JES/167/144502/mmedia). A hydrophilic Zirfon® membrane from Agfa-Gevaert N.V. was used to reduce the electrolyte pressure on the samples. The glass fiber fleece soaked in 0.1 M KOH followed after the Zirfon® membrane and after the fleece followed the sample. A Nickel mesh was used as current collector. The working electrode was the sample, a platinum electrode was used as counter electrode and a Hg/HgO (1 M NaOH) electrode was used as reference electrode. Oxygen supply of 1 N l min^{-1} was connected to the half-cell during the measurement.

Since a symmetrical setup was applied for galvanostatic measurements, the resulting voltage $U_{\max}$ is the sum of the absolut overpotentials for each reaction η_{OER} and η_{ORR} (1). This is independent of the current direction. The total resistance (R_{total}) was calculated from results of galvanostatic cycling by applying *Ohm's* law (2). Ohmic resistance or iR-drop, respectively, (R_{ohm}) was measured by impedance spectroscopy. Subsequently, R_{ohm} was subtracted from R_{total} to get the sum of polarization and diffusion resistance (R_{PD}) as outcome (3):

$$U_{\max} = |\eta_{OER}| + |\eta_{ORR}| + IR_{Ohm} + IR_{Diffusion} \quad [1]$$

$$R_{total} = \frac{U_{\max}}{I_{applied}} \quad [2]$$

$$R_{PD} = R_{total} - R_{ohm} \quad [3]$$

Furthermore, the specific surface area (S_{BET}) was multiplied with MnO_x mass (4) to calculate the absolute surface area (A_{SBET}). The

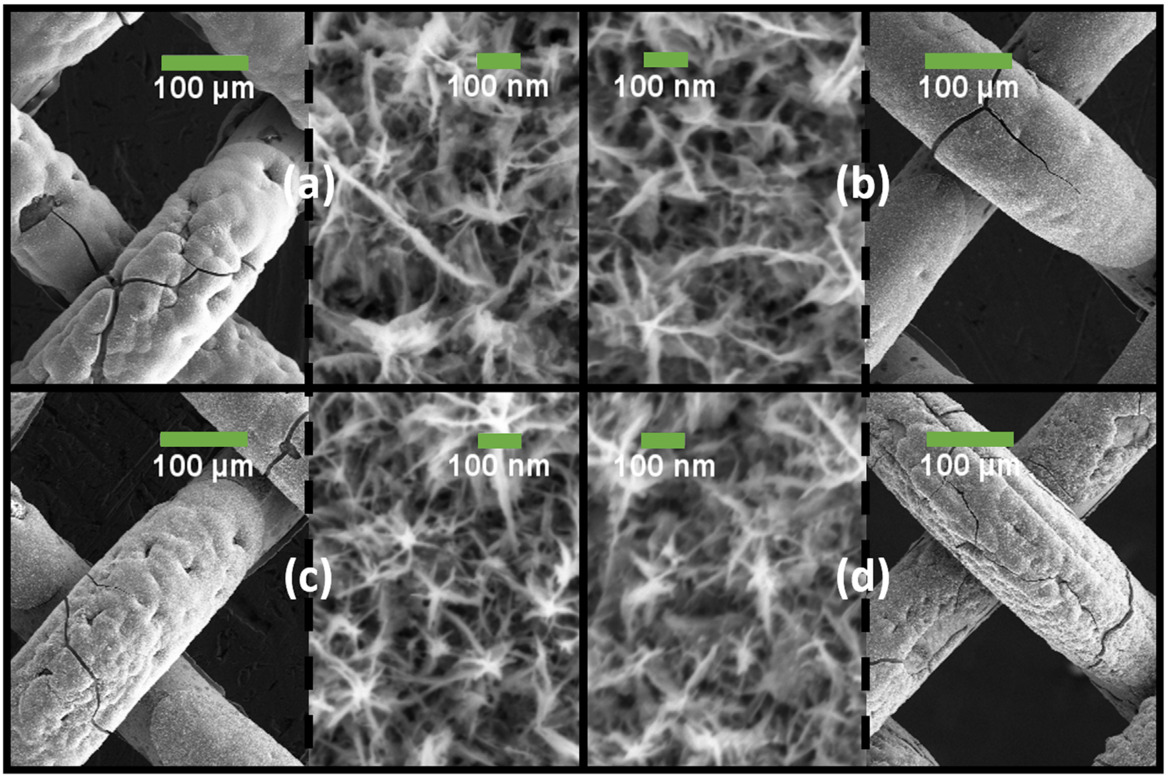

Figure 2. SEM image of electrodeposited MnO_x on nickel mesh in nano- and micrometer range at different r_{scan}: (a) Scr1; (b) Scr2; (c) Scr3; (d) Scr4.

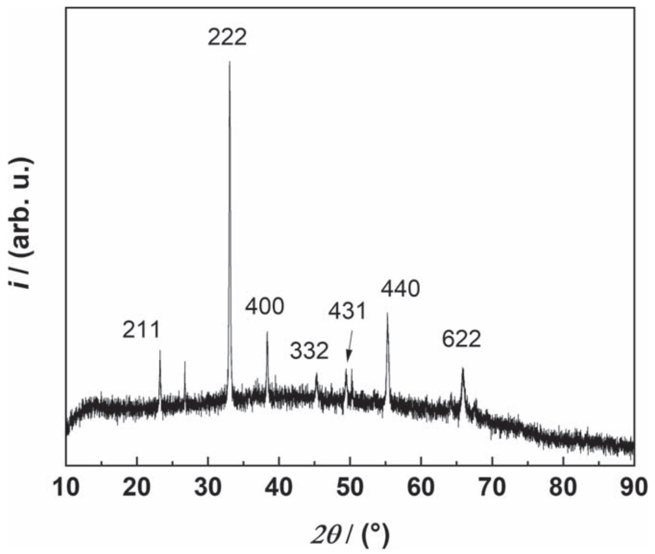

Figure 3. XRD pattern of electrodeposited MnO_x (Mn_2O_3-bixbyite-c, JCPDS #00-041-1442).

polarization and diffusion resistance (R_{PD}) was divided by the geometric surface area A_{geo} (5) to calculate geometric surface area normalized resistance (nR_{geo}). In the following are the formulas:

$$A_{SBET} = S_{BET} * m_{MnOx} \quad [4]$$

$$nR_{geo} = \frac{R_{PD}}{A_{geo}} \quad [5]$$

The deposited mass was calculated (6) in specific mass (m_{geo}) by the division of m_{MnO_x} and the geometric surface area (A_{geo}):

$$m_{geo} = \frac{m_{MnO_x}}{A_{geo}} \quad [6]$$

Results and Discussion

Surface characterization.—The surfaces of samples were investigated by FESEM after hydrophobic treatment and electrodeposition.

Figure 2 depict MnO_x coated nickel meshes from deposition at different scan rates (r_{scan}). All samples exhibit a star-like and porous structure in the nanometer range. Thus, it is assumed that the morphology of the MnO_x layers is independent from the r_{scan} variations in that range. The structure is similar to the star fruit structure of *Chou's* group.[10] In the micrometer range, the coatings differ significantly. All samples show cracks and cavities in different intensities but sample Scr2 (Fig. 2b) exhibits the smoothest surface. This indicates a difference in their macroscopic surface area. In general, the highest possible active surface area is preferable and is achieved by surfaces with a higher degree of structuring in comparison to smooth surfaces. The exhibited surface area is investigated with nitrogen sorption (BET) and cycling voltammetry (CV) measurements.

For all samples, the region nearby the overlapping nickel wires remained mostly uncoated. It is assumed that the hydrophobic properties of the meshes caused a trapping of small air bubbles in that region. This led to electrochemically inaccessibility of this surface area for the coating process. However, sample Scr4 (Fig. 2d) does not clearly show these similarities. It is assumed that due to the high r_{scan} of $50\,\mathrm{mV\,s^{-}}$ the trapped air bubbles behave different compared to the other samples during the electrodeposition. Other parameters were not varied. This occurrence of trapped air bubbles and their behavior at different r_{scan} during electrodeposition was not further investigated.

The catalyst layer thickness is apparent at the uncoated area nearby the overlapping nickel wire (Fig. A2: magnification of Fig. 2, shown in Appendix). Figures A2b to A2d shows the declining layer thickness with rising r_{scan}. However, the sample shown in Fig. A2a indicates a slightly uneven thickness.

Stearic acid is visible as dark points as proven by EDS analysis (Fig. A3, shown in Appendix). However, before the electrochemical treatment it is not visible on those samples (Fig. A1, shown in Appendix). This indicates some kind of chemical reaction of stearic acid during electrochemical deposition. The mechanism of the chemical reaction was not investigated in this work.

The electrodeposited MnO_x exhibit a XRD pattern which can be assigned to Mn_2O_3-bixbyite-c (Fig. 3). Its reflexes are at $2\theta = 23.2°$, 33,0°, 38.3°, 45.3°, 49.3°, 55,2° and 65.8°. A similar XRD pattern for Mn_2O_3 was also obtained by *Pudukudy*'s group[27] and *Menezes's* group.[28] Since their MnO_x-materials were calcined after synthesis, higher degrees of crystallinity were obtained. However, there are minor reflexes which can be assigned to other structures. Due to the low reflex-to-noise ratio, it was only possible to observe the largest reflex of these side phases. One possible structure is sodium manganese sulfate hydrate ($Na_2Mn(SO_4)_2$ H_2O, JCPDS #00-020-1127). This structure exhibits their main diffraction reflexes at $2\theta =$ 26.7° and 29.8°. But the second main peak is probably within the

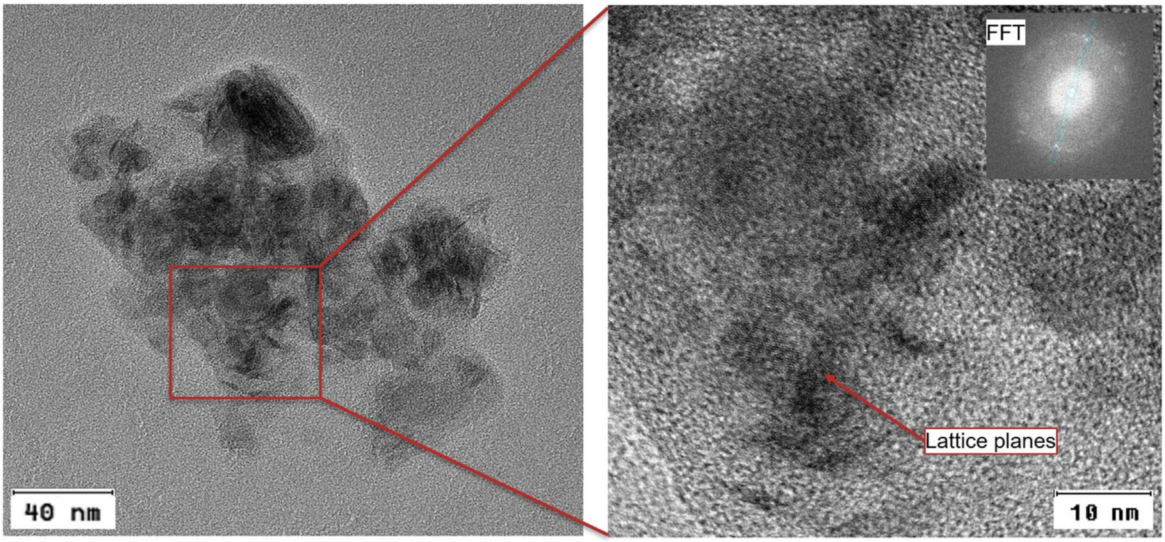

Figure 4. TEM images of electrodeposited MnO_x particles at different orders of magnitude and with a fast Fourier transformation (FFT).

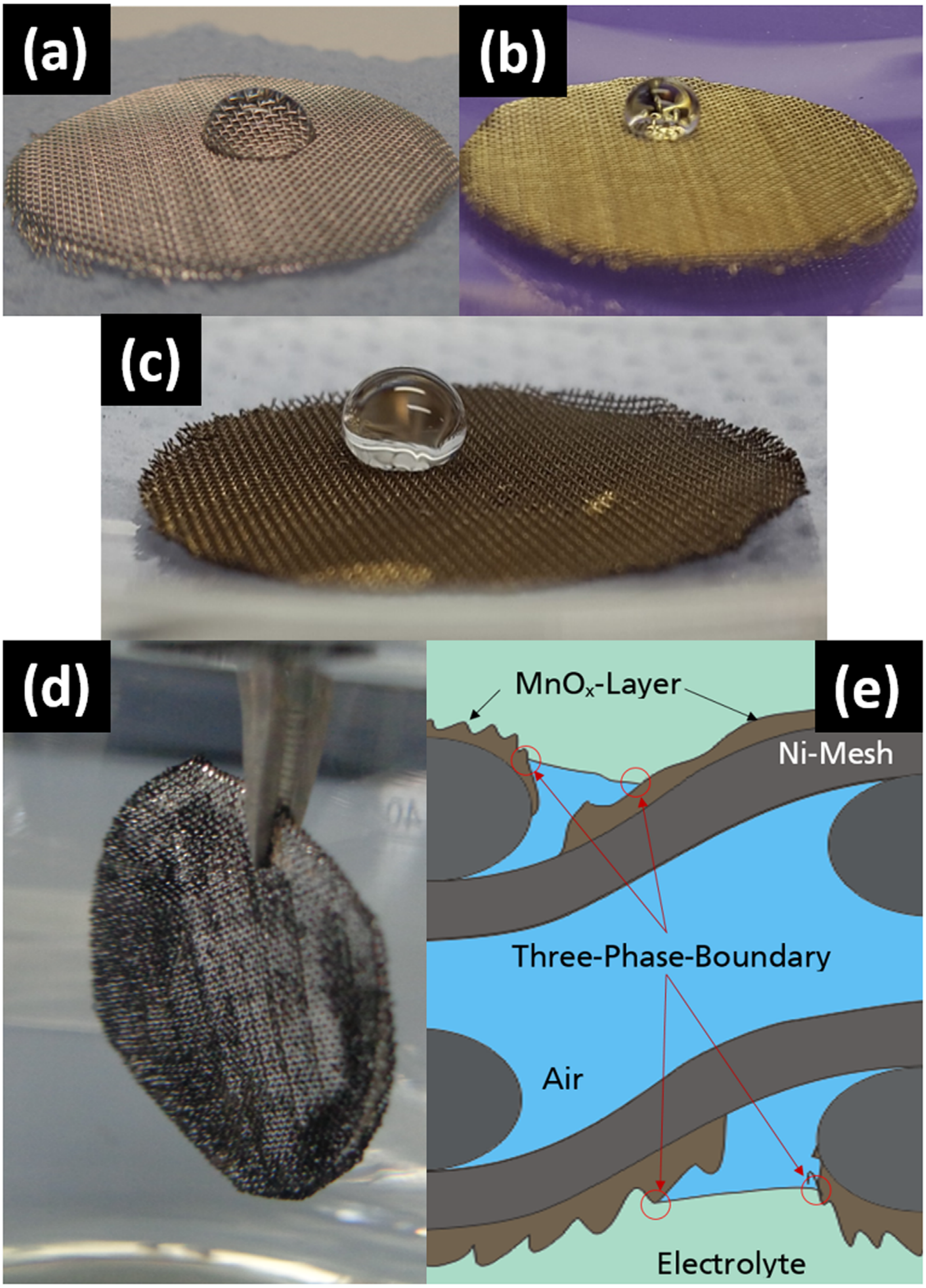

Figure 5. Images of nickel meshes which were (a) only cleaned in ethanol, (b) hydrophobic treated and (c) after hydrophobic treatment and coated with MnO_x, (d) image of a double electrode design fully immersed in deionized water and (e) schematic depiction of three phase boundary at the double electrode design when fully immersed.

background noise. Furthermore, all possible chemical combinations of the element's sodium, sulphur, oxygen, manganese, hydrogen and nickel and their XRD patterns were analyzed but the reflex at $2\theta = 50.2°$ could not be assigned properly. This might be, due to the background noise which indicates a great amount of X-ray amorphous substances, and therefore it is implied, that the coating consists not only of pure Mn_2O_3. This might be explained by other, unidentified crystalline structures, small crystallites or amorphous MnO_x.

TEM images from MnO_x (Fig. 4) indicate different morphologies and a high polycrystallinity since a number of differently orientated lattice planes are observable (Fig. 4, right). This was already implied by XRD.

The fast *Fourier* transform (FFT) give only weak reflexes which also highlights the amorphousness of the material. Still, FFT of the respective TEM images give in the specific lattice constants or interplanar distances, respectively. These can be compared with distances deduced from XRD.

The comparison of the calculated with the measured results (Table AI in the Appendix) shows that the reflexes at $2\theta = 33°$, 49.3°/50.2° and 55.2° have the highest match. The reflexes $2\theta = 49.3°$ and 50.2° have interplanar distances which are very close to

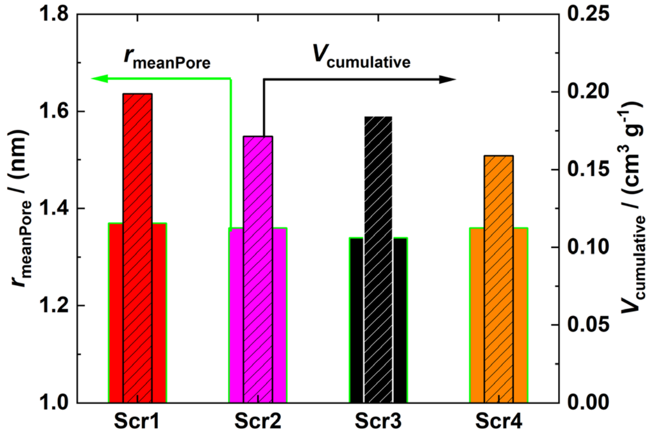

Figure 6. Mean pore distribution (MP-method) of all mesh samples (Scr1: 12.5 mV s^{-1}; Scr2: 25 mV s^{-1}; Scr3: 37.5 mV s^{-1}; Scr4: 50 mV s^{-1}; $r_{meanPore}$: mean pore size (without hatching); $V_{cumulative}$: cumulative pore volume of MnO_x (with hatching)).

Table II. Results from characterization regarding deposition condition, mass, specific mass, contact angle, specific surface area, geometric and BET surface area.

Sample	Scr1	Scr2	Scr3	Scr4	GDE_{ref}
r_{scan}/mV s^{-1}	12.5	25	37.5	50	/
m_{MnOx}/mg	21.4	17.0	11.4	9.8	59.2
m_{geo}/mg cm^{-2}	5.2	4.1	2.7	2.4	13.1
CA/°	64.5	89.7	118.1	126.0	139.2
S_{BET}/m^2 g^{-1}	140.1	64.8	36.4	21.6	233.1
A_{SBET}/m^2	3.0	1.1	0.4	0.2	13.8
A_{geo}/cm^2	4.2	4.2	4.2	4.2	4.5

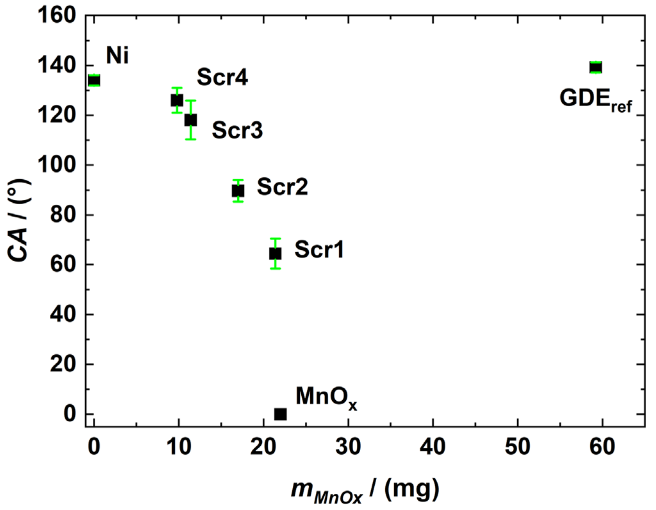

Figure 7. Dependency of electrodeposited MnO_x mass on hydrophobicity compared with commercial GDE (GDE_{ref}); (Ni: hydrophobic treated and uncoated nickel mesh; MnO_x: electrochemically coated nickel sheet; number of repetitions: 3).

each other. Due to that, it is difficult to determine which reflex is more significant. These reflex signals could be also only one signal. However, the evaluation of the data showed a match with MnO_x XRD pattern reflexes at $2\theta = 33°$, 49.3°/50.2° and 55.2°. Thus, it can be concluded that besides smaller domains with measurable crystallinity (Mn_2O_3), the deposited material is largely amorphous MnO_x.

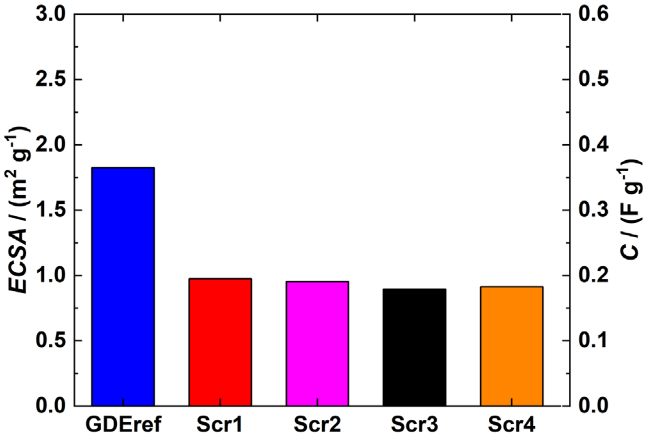

Figure 8. Electrochemical specific surface area and specific capacitance of all samples.

Furthermore, according to the *Pourbaix*[26] diagram of manganese the variation of the electrodeposition scan rate (r_{scan}) has no influence on the deposited MnO_x species. The XRD of all presented MnO_x samples is shown exemplarily in Fig. 3. The structure and morphology of deposited MnO_x (Fig. 4) is promising for the application in an OER/ORR gas diffusion electrode.

Figures 5a–5c show exemplarily samples of differently treated nickel meshes with drops of deionized water on top. It is apparent that the hydrophobicity is influenced significantly by the hydrophobic treatment (b) and electrodeposition (c). Furthermore, two hydrophobic nickel meshes were joined together to increase the surface area that can be coated with MnO_x (Fig. 5d). The formation of a silvery film of air will result by immersing this coated double electrode design in deionized water (Fig. 5d).

Air is trapped between the two hydrophobic nickel meshes and forms an internal three phase boundary (Fig. 5e red circles) according to the *Cassie & Baxter* model.

All nitrogen sorption isotherm linear plots of the mesh samples (Fig. A7) exhibit the same hysteresis loop type, which indicates the existence of disordered micropores. Thus, the micropore analysis method (MP-method) was used to determine the pore size distribution (Fig. A8).

All mesh samples achieved approx. the same mean pore size (Fig. 6) of about 1.34–1.37 nm. However, the cumulative pore volume is influenced by the deposition scan rate (r_{scan}). The highest volume exhibited Scr1 (0.19 cm^3 g^{-1}) which is followed by Scr3 (0.18 cm^3 g^{-1}), then by Scr2 (0.17 cm^3 g^{-1}) and at last by Scr4 (0.16 cm^3 g^{-1}). In general, with a lower r_{scan} a higher cumulative pore volume was showed.

The influence of the scan rate (r_{scan}) on deposited mass, contact angle, specific surface area (S_{BET}) and absolute surface area (A_{SBET}) is shown in Table II. The deposited mass and the contact angle or hydrophobicity, respectively, are directly proportional but the deposited mass and S_{BET} are indirectly proportional to the r_{scan} (Figs. A4 and A5, shown in Appendix).

Figure 7 shows the dependency of deposited MnO_x mass on hydrophobicity including data from a commercial GDE (GDE_{ref}). Contact angle decreases with increasing MnO_x mass on hydrophobic Nickel mesh. The highest contact angle of the coated samples was observed for Scr4 (126°), which has the lowest MnO_x mass (9.8 mg). Hydrophobic treated and uncoated Nickel mesh (134°) exhibits nearly the same contact angle like GDE_{ref} (139°). A nickel sheet was electrochemically coated with MnO_x at a r_{scan} of 50 mV s^{-1} to analyze the intrinsic contact angle of MnO_x. This sample exhibits a contact angle of 0 and therefore MnO_x is hydrophilic. This indicates that the deposited MnO_x causes the reduction of hydrophobicity. A comparison of the SEM measurements (Fig. 2, Figs. A1 and A2) indicates that the surface roughness of the coated samples is higher

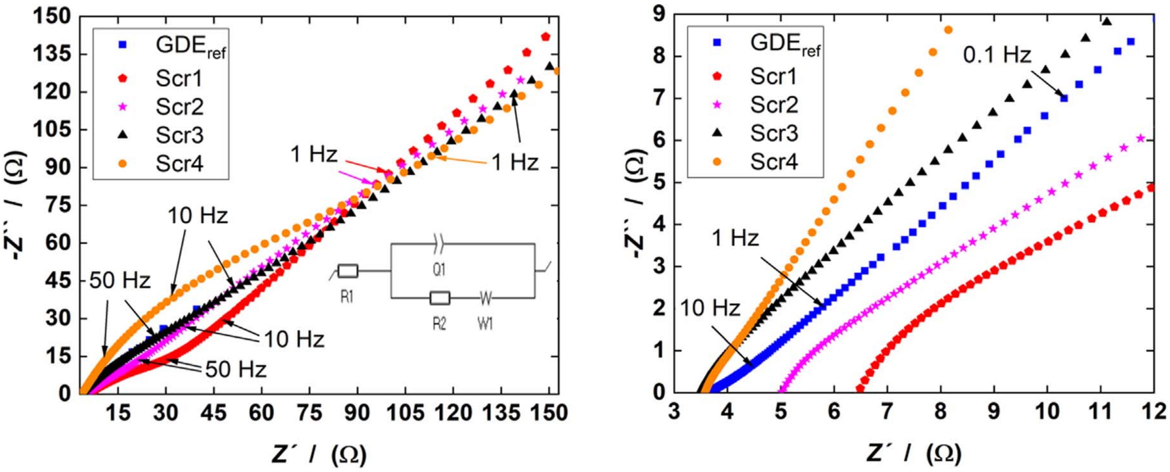

Figure 9. Impedance spectroscopy measurement Nyquist plot overview at a frequency range of 69 kHz—approx. 0.5 Hz, (left) and zoom-in of the respective measurements (right). Image of equivalent circuit for fitting the impedance results (R_1: ohmic resitance; R_2: polarization resistance; W_1: Warburg-Element/ diffusive resistance; Q_1: constant phase element).

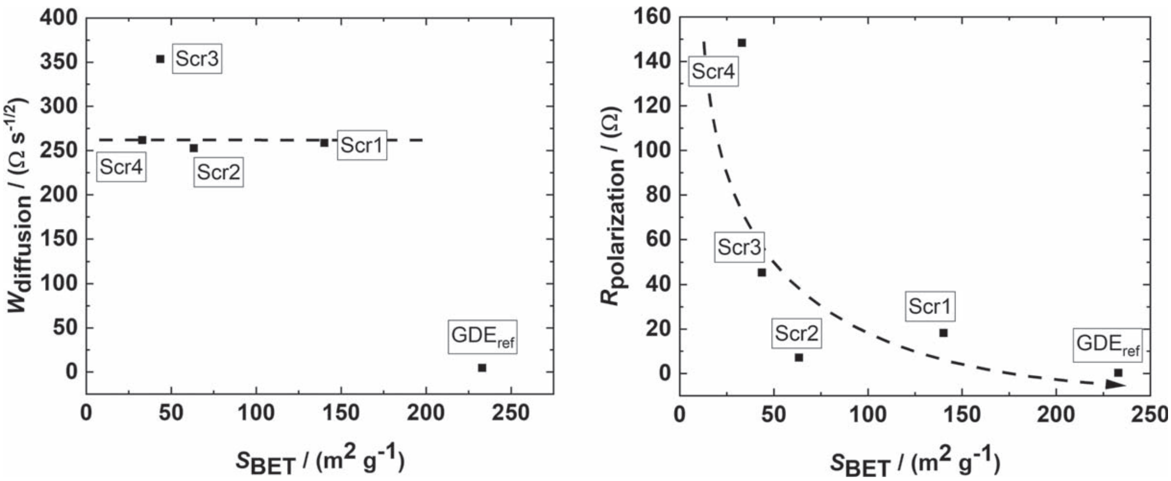

Figure 10. Determined polarization (right) and diffusion (left) resistances in dependence of S_{BET}. Dashed lines for visual guidance.

than the uncoated one. However, there is no increase of hydrophobicity by surface roughness of deposited MnO_x.

Furthermore, the electrochemical deposition of MnO_x has an impact on the stearic acid (Fig. A3, shown in Appendix). It is assumed that the organic structure of stearic acid is altered by electrodeposition, which possibly influenced the hydrophobicity. The alteration increases over deposition-time and due to that by low r_{scan}. If r_{scan} is low, more potential steps per second are needed to finish the potentiodynamic cycling between 0.3 V and 0.6 V. This assumption was not further investigated. In general, the hydrophobicity of the coated samples is supported by stearic acid but is decreased by hydrophilic MnO_x mass.

It was assumed that if the electrode has isolated laying catalyst sites which are distributed over a hydrophobic surface, there will be sufficient three phase boundary (Fig. 5d). Thus, before the electrodeposition of MnO_x the Nickel mesh was made hydrophobic in order to transfer this property to the final GDE. The deposition of MnO_x occurs where the electrical conductivity of the hydrophobic surface and the contact to the electrolyte is sufficient. However, there is a trade-off between hydrophobicity and electrodeposition. In general, hydrophobic treatments of metallic surfaces are done to increase their corrosion resistance or reduce the electrochemical reactions on their surface, respectively.[24,25] That means there is a hindrance of electrodeposition processes on the surface due to the hydrophobicity of nickel meshes. This is indicated by the comparison of the coated nickel sheet (marked as MnO_x in Fig. 7) and Scr4, which are both coated with 50 mV s^{-1}. The untreated nickel sheet exhibits more than twice the MnO_x mass of Scr4. A deeper understanding of the interaction between hydrophobicity and electrodeposited catalyst would need further investigation.

Electrochemical characterization.—In Fig. 8, the electrochemical specific surface area (*ECSA*) and specific capacitance (*C*) of all samples are shown. The *ECSA* of GDE$_{ref}$ is approx. twice as large as the *ECSA* of all carbon free samples. Additionally, GDE$_{ref}$ shows that it can carry approx. twice the amount of charge compared to the carbon free GDEs due to the specific capacitance results. It is assumed that GDE$_{ref}$ provides due to its electrode build up (porous carbon main body) much more electrochemical active sites. Almost all the coated samples exhibited the same value of approx. 1 m^2 g^{-1} and 0.2 F g^{-1}. Thus, there is no influence of scan rate (r_{scan}) on the electrochemical accessible surface area as found for the S_{BET} (Table II). The cause of this difference must be investigated. It is noteworthy that, for all samples, the found *ECSA* is orders of magnitude smaller than S_{BET}. In general, the BET measurement uses nitrogen gas to fill the pores and by that to determine the specific surface area. But the *ECSA* or specific capacitance, respectively, is determined by the aqueous electrolyte (KOH) which is in contact with an electrochemical active site of the sample. It is assumed that the hydrophobicity of carbon free GDEs and GDE$_{ref}$ influenced the

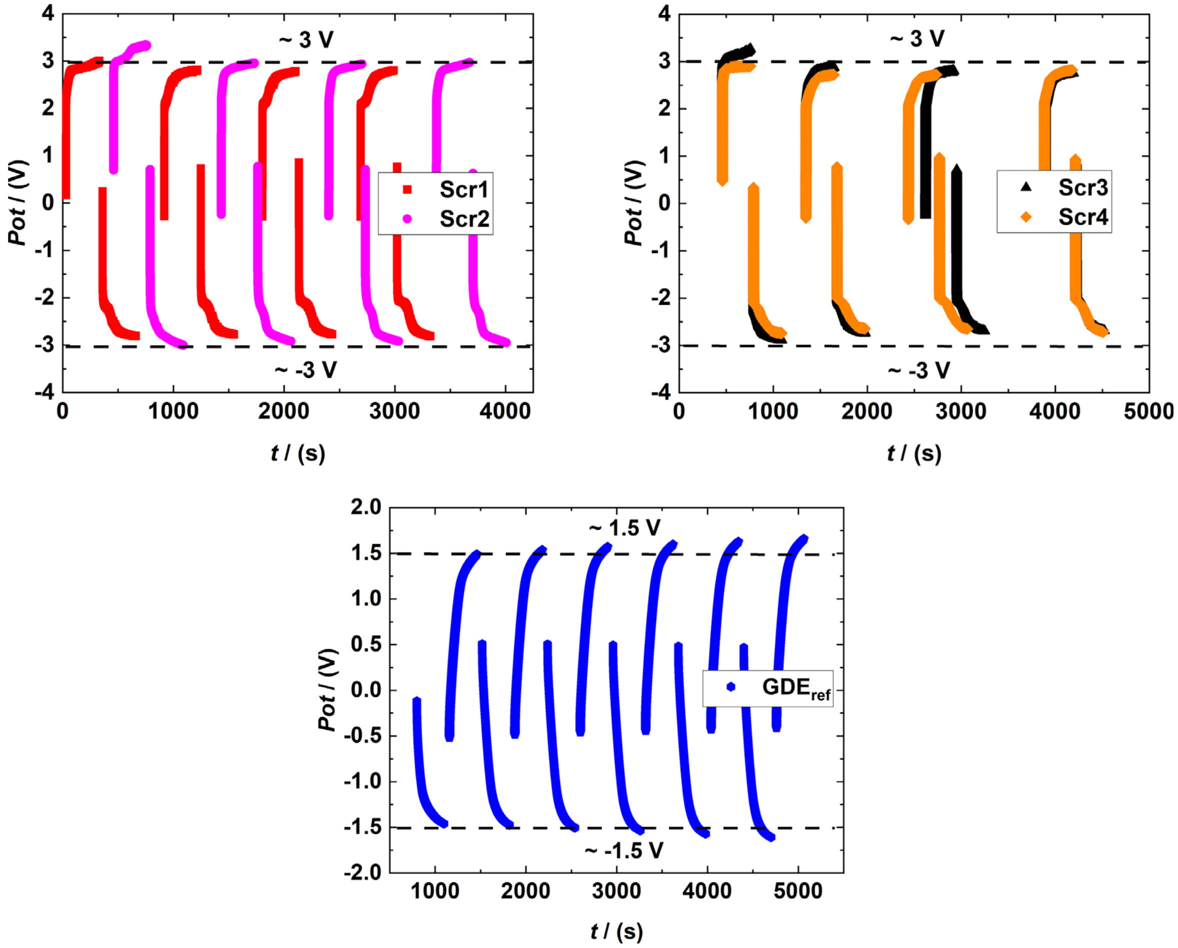

Figure 11. Image of galvanostatic cycling results of all carbon free GDE samples and GDE$_{ref}$ at ±10 mA cm^{-2} and each lasted for 5 min.

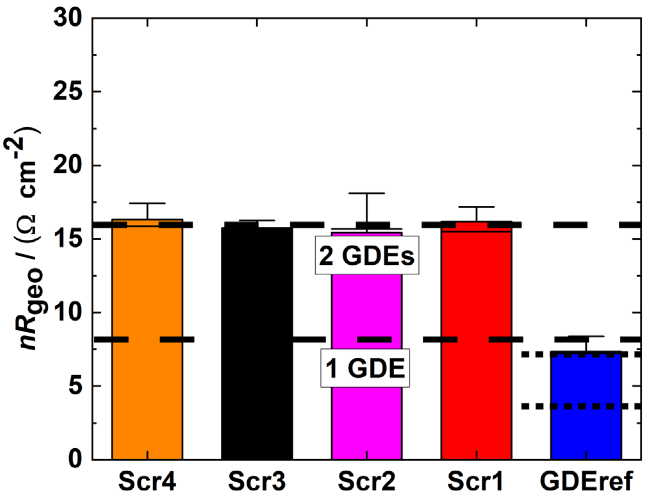

Figure 12. Polarization and diffusion resistance determined by galvanostatic cycling at 10 mA cm^{-2}, geometric normalized resistance nR$_{geo}$ (dashed lines are indicating the results of two GDEs and only one).

electrolyte contact to the electrochemical active sites but had no influence on nitrogen sorption. Thus, it is assumed that this difference is caused by the different measurement concepts.

Impedance spectroscopy was measured with the symmetric cell assembly. The results are summarized in *Nyquist* plot in Fig. 9. The electrode sample prepared with the lowest r_{scan} (12.5 mV s^{-1}, Scr1) exhibits with 6.5 Ω the highest ohmic resistance. This can be explained by the comparatively high amount of MnO$_x$ and the arising insulation by MnO$_x$. The shapes of all *Nyquist* plots indicate the presence of a polarization and a diffusive resistance. The polarization resistance is evident by the implied semi-circle for each sample. Since as symmetric cell assembly was applied, this resistance can be understood as the charge transfer resistance for oxygen reduction and oxidation. The implied polarization resistance increases with increasing r_{scan} (Table AII and Fig. 9). This indicates the influence of decreasing deposited catalyst mass. An approximately 45° slope in the *Nyquist* plot is evident with decreasing frequency, which indicates the diffusive resistance (Fig. 9, left). The impedance results were fitted with the equivalent circuit showed in Fig. 9, left in the *Nyquist* plot.

Polarization resistance and *Warburg* diffusion were determined by fitting the raw data to the equivalent circuit shown in Fig. 9 (left) in the *Nyquist* plot. The results are summarized in Table AII. The Warburg diffusion (Fig. 10, left) of all samples amounts roughly 257 Ω s$^{-1/2}$. Scr3 is assumed to be an outlier because all other samples exhibited approx. the same $W_{diffusion}$ (Fig. 10, left) and *ECSA* (all mesh samples, Fig. 8) values despite of the increasing S_{BET} (Table II) values (Scr4 < Scr3 < Scr2 < Scr1).

This unchanging, comparatively high *Warburg* diffusion coefficients are indicating the influence of the thin electrolyte film on the electrochemical activity of the GDE. Oxygen is diffusing into the electrolyte and vice versa at this thin electrolyte film or gas-liquid interface, respectively. It can be assumed that the thickness of GDE electrolyte film led to an increased diffusion length of dissolved oxygen, and therefore, an increased *Warburg* diffusion coefficient was found.[29–31] It might be concluded that for all MnO$_x$ samples the thickness of the diffusion layer (through the electrolyte to the electrochemical active sites) results in the respective *Warburg* diffusion coefficients (Fig. 10, left).

It was observed, that after the electrochemical measurement the samples were completely wetted with the electrolyte. This indicates the hydrophobicity and porosity of coated meshes were inadequate for forming an effective three phase boundary. Thus, the whole reaction might be limited by the oxygen diffusion layer thickness. It is presumed that by increasing the hydrophobicity, porosity and mesh density, the diffusion layer thickness will be reduced. However, the problem of diffusion of oxygen is known as a difficult part also for state of the art GDE.[32]

Since the electrochemical surface area ECSA stayed unaltered over all samples it might be concluded that determination of the ECSA via cyclic voltammetry is not sufficient for porous manganese oxide. Therefore, S_{BET} was taken as reference point. The polarization resistance decreases with rising S_{BET} (Table II and Fig. 10, right). This reduction is presumably caused by higher distribution of possibly available electrochemical active sites on the catalysts.

In Fig. 11 the galvanostatic cycling at $\pm 10\ \mathrm{mA\ cm^{-2}}$ are shown. The carbon free GDE samples are between ±3 V and the $\mathrm{GDE_{ref}}$ sample is between $+1.5$ V and -1.5 V. Both reactions (OER and ORR) are present at -10 or $10\ \mathrm{mA\ cm^{-2}}$ because a symmetric cell setup was used. Here, the counter and working electrode were equipped with the GDE under investigation. Thus, the electrical potential at $\pm 10\ \mathrm{mA\ cm^{-2}}$ is the sum of OER *and* ORR potential of two electrodes. A direct examination of the bifunctionality of the GDE towards OER and ORR is hereby possible. The comparison of all results shows that the combined OER/ORR potential of $\mathrm{GDE_{ref}}$ increased with each cycle. This behavior can be possibly caused by the corrosion of carbon, which lead to a decrease of conductivity and loss of catalyst/carbon connections. Furthermore, all carbon free samples show an asymptotic approach and at the end an almost stable electrical potential course. This indicates that the ionic transport of $\mathrm{OH^-}$ and dissolved oxygen is sufficient.

In Fig. 12 the normalized resistances of carbon free samples are compared with $\mathrm{GDE_{ref}}$. The geometric normalized resistance (nR_{geo}) values are calculated from the galvanostatic results (Fig. 11), the ohmic resistance (iR-drop, impedance spectroscopy results) and the geometric surface area. These results are from two GDEs, where both processes (OER and ORR) were simultaneously present, due to the symmetric cell setup. Thus, the exhibited results must be halved to get the values for one GDE. The dashed lines are indicating this (Fig. 12). $\mathrm{GDE_{ref}}$ exhibits the lowest nR_{geo} value ($\sim 3.5\ \Omega\ \mathrm{cm^{-2}}$), which can be explained by its hydrophobicity (Table II) and fine porous structure. These properties support sufficient diffusion and accessibility of electrochemical active sites. All mesh samples show similar nR_{geo} values of $\sim 8\ \Omega\ \mathrm{cm^{-2}}$. Thus, there is no noticeable influence of scan rate (r_{scan}) on nR_{geo}.

It is assumed that the diffusion is the major bottleneck for the OER/ORR of all prepared samples due to the similarity of constant $n\mathrm{R_{geo}}$ and constant $W_{\mathrm{diffusion}}$ while the polarization resistance changes in between samples (Fig. 10). Thus, it is necessary to reduce the diffusion resistance for these hydrophobic mesh samples.

Conclusions

Carbon free gas diffusion electrodes (GDE) were prepared, characterized and compared to a commercially available standard carbon based GDE ($\mathrm{GDE_{ref}}$). A nickel mesh as electrode body was hydrophobized and was subsequently electrochemically coated with $\mathrm{MnO_x}$. The scan rate (r_{scan}) of the electrodeposition of $\mathrm{MnO_x}$ was varied to alter the catalysts macro surface structure, the pore size distribution and the catalyst mass on the nickel mesh.

All samples were electrochemically analyzed in a symmetric cell setup. Impedance spectroscopy reveals large and constant *Warburg* diffusion coefficients for all r_{scan} but decreasing polarization resistances with lower r_{scan}. However, galvanostatic measurements at $\pm 10\ \mathrm{mA\ cm^{-2}}$ showed an asymptotic electric potential approach towards stable course of the carbon free GDEs. This indicates that the bifunctionality and mass-transport are present and able to manage this current density. These results were converted to area-normalized polarization and diffusion resistance (nR_{geo}), which showed that the diffusion part is the major contributor to the resistance for all prepared samples.

The specific surface area (BET) of the catalyst increased with lower r_{scan} due to the increasing deposition time at low r_{scan}. However, the electrochemical accessible specific surface area or specific capacitance, respectively, exhibited the same values for all carbon free samples. These results support the conclusion that the major contributor for the total resistance is the diffusion for the presented carbon free samples.

The results shown complement the work of other groups, which are working on the carbon free GDE topic and allow an insight at a different perspective.

Acknowledgments

This work was supported by the scholarship of *Reiner Lemoine* foundation.

ORCID

Artur Bekisch https://orcid.org/0000-0002-1448-2317

References

1. S. Park, J.-W. Lee, and B. N. Popov, "A review of gas diffusion layer in PEM fuel cells: materials and designs." *Int. J. Hydrogen Energy*, **37**, 5850 (2012).
2. R. A. Tufa, E. Rugiero, D. Chanda, and J. Hnàt, "Salinity gradient power-reverse electrodialysis and alkaline polymer electrolyte water electrolysis for hydrogen production." *J. Membr. Sci.*, **514**, 155 (2016).
3. J. Pan, Y. Y. Xu, H. Yang, Z. Dong, H. Liu, and B. Y. Xia, "Advanced architectures and relatives of air electrodes in Zn-Air batteries." *Advanced Science (Weinheim, Baden-Wurttemberg, Germany)*, **5**, 1700691 (2018).
4. R. Amirante, E. Cassone, E. Distaso, and P. Tamburrano, "Overview on recent developments in energy storage: mechanical, electrochemical and hydrogen technologies." *Energy Convers. Manage.*, **132**, 372 (2017).
5. A. B. Gallo, J. R. Simões-Moreira, H. K. M. Costa, M. M. Santos, and E. Moutinho dos Santos, "Energy storage in the energy transition context: a technology review." *Renew. Sustain. Energy Rev.*, **65**, 800 (2016).
6. M. Götz, J. Lefebvre, F. Mörs, A. McDaniel Koch, F. Graf, S. Bajohr, R. Reimert, and T. Kolb, "Renewable power-to-gas: a technological and economic review." *Renewable Energy*, **85**, 1371 (2016).
7. M. Tahir, L. Pan, F. Idrees, X. Zhang, L. Wang, J.-J. Zou, and Z. L. Wang, "Electrocatalytic oxygen evolution reaction for energy conversion and storage: a comprehensive review." *Nano Energy*, **37**, 136 (2017).
8. K. Zhang, X. Han, Z. Hu, X. Zhang, Z. Tao, and J. Chen, "Nanostructured Mn-based oxides for electrochemical energy storage and conversion." *Chem. Soc. Rev.*, **44**, 699 (2015).
9. X. Fang, X. Lu, X. Guo, Y. Mao, Y.-S. Hu, J. Wang, Z. Wang, F. Wu, H. Liu, and L. Chen, "Electrode reactions of manganese oxides for secondary lithium batteries." *Electrochem. Commun.*, **12**, 1520 (2010).
10. S. Chou, F. Cheng, and J. Chen, "Electrodeposition synthesis and electrochemical properties of nanostructured γ-MnO2 films." *J. Power Sources*, **162**, 727 (2006).
11. Y.-C. Tsai, W.-D. Yang, K.-C. Lee, and C.-M. Huang, "An effective electrodeposition mode for Porous $\mathrm{MnO_2}$/Ni foam composite for asymmetric supercapacitors." *Materials (Basel, Switzerland)*, **9**, 246 (2016).
12. P. H. Benhangi, A. Alfantazi, and E. Gyenge, "Manganese dioxide-based bifunctional oxygen reduction/evolution electrocatalysts: effect of Perovskite doping and potassium ion insertion." *Electrochim. Acta*, **123**, 42 (2014).
13. E. Fabbri, A. Habereder, K. Waltar, R. Kötz, and T. J. Schmidt, "Developments and perspectives of oxide-based catalysts for the oxygen evolution reaction." *Catal. Sci. Technol.*, **4**, 3800 (2014).
14. A. S. Ryabova et al., "Rationalizing the Influence of the Mn(IV)/Mn(III) Red-Ox transition on the electrocatalytic activity of manganese oxides in the oxygen reduction reaction." *Electrochim. Acta*, **187**, 161 (2016).
15. L.-A. Stern and X. Hu, "Enhanced oxygen evolution activity by NiOx and Ni(OH)2 nanoparticles." *Faraday Discuss.*, **176**, 363 (2014).
16. C. C. L. McCrory, S. Jung, J. C. Peters, and T. F. Jaramillo, "Benchmarking heterogeneous electrocatalysts for the oxygen evolution reaction." *JACS*, **135**, 16977 (2013).
17. C. C. L. McCrory, S. Jung, I. M. Ferrer, S. M. Chatman, J. C. Peters, and T. F. Jaramillo, "Benchmarking hydrogen evolving reaction and oxygen evolving reaction electrocatalysts for solar water splitting devices." *Journal of the American Chemical Society*, **135**, 4347 (2015).
18. Z.-L. Wang, D. Xu, J.-J. Xu, and X.-B. Zhang, "Oxygen electrocatalysts in metal-air batteries: from aqueous to nonaqueous electrolytes." *Chem. Soc. Rev.*, **43**, 7746 (2014).
19. P. Gu, M. Zheng, Q. Zhao, X. Xiao, H. Xue, and H. Pang, "Rechargeable zinc–air batteries: a promising way to green energy." *J. Mater. Chem. A*, **5**, 7651 (2017).

20. D. U. Lee, P. Xu, Z. P. Cano, A. G. Kashkooli, M. G. Park, and Z. Chen, "Recent progress and perspectives on bi-functional oxygen electrocatalysts for advanced rechargeable metal–air batteries." *J. Mater. Chem. A*, **4**, 7107 (2016).
21. F. Moureaux, P. Stevens, G. Toussaint, and M. Chatenet, "Development of an oxygen-evolution electrode from 316L stainless steel: application to the oxygen evolution reaction in aqueous lithium–air batteries." *J. Power Sources*, **229**, 123 (2013).
22. J. W. D. Ng, M. Tang, and T. F. Jaramillo, "A carbon-free, precious-metal-free, high-performance O2 electrode for regenerative fuel cells and metal–air batteries." *Energy Environ. Sci.*, **7**, 2017 (2014).
23. K. Xu, A. Loh, B. Wang, and X. Li, "Enhancement of oxygen transfer by design nickel foam electrode for zinc−air battery." *J. Electrochem. Soc.*, **165**, A809 (2018).
24. H. Jie, Q. Xu, L. Wei, and Y. Min, "Etching and heating treatment combined approach for superhydrophobic surface on brass substrates and the consequent corrosion resistance." *Corros. Sci.*, **102**, 251 (2016).
25. W. Liu, Q. Xu, J. Han, X. Chen, and Y. Min, "A novel combination approach for the preparation of superhydrophobic surface on copper and the consequent corrosion resistance." *Corros. Sci.*, **110**, 105 (2016).
26. M. Pourbaix, *Atlas of Electrochemical Equilibria in Aqueous Solutions* (Nat'L Assoc. of Corrosion, Printed in the USA by National Association of Corrosion Engineers, 1440 South Creek Drive Houston, Texas 77084) Second English Edition 1974 ed. (1974), Library of Congress Catalog Card No. 65-11670.
27. M. Pudukudy and Z. Yaakob, "Synthesis, characterization, and photocatalytic performance of Mesoporous α-Mn2O3 microspheres prepared via a precipitation route." *Journal of Nanoparticles*, **2016**, 1 (2016).
28. P. W. Menezes, A. Indra, P. Littlewood, M. Schwarze, C. Göbel, R. Schomäcker, and M. Driess, "Nanostructured manganese oxides as highly active water oxidation catalysts: a boost from manganese precursor chemistry." *ChemSusChem*, **7**, 2202 (2014).
29. M. Röhe, F. Kubannek, and U. Krewer, "Processes and their limitations in oxygen depolarized cathodes: a dynamic model-based analysis." *ChemSusChem*, **12**, 2373 (2019).
30. F. G. Will and D. J. BenDaniel, *Significance of Electrolyte Films for Performance of Porous Hydrogen Electrodes I. Film Model.* (The Electrochemical Society, Generel Electric Research and Development Center, Schenectady, New York) 116, 933 (1969).
31. P. Björnbom, "Modelling of a double-layered PTFE-bonded oxygen electrode." *Electrochim. Acta*, **32**, 115 (1987).
32. F. Kubannek, T. Turek, and U. Krewer, "Modeling oxygen gas diffusion electrodes for various technical applications." *Chem. Ing. Tech.*, **2019**, 1 (2019).